Int. J. Electrochem. Sci., 15 **(2020)** 10157 – 10172, doi: 10.20964/2020.10.24

International Journal of
ELECTROCHEMICAL
SCIENCE
www.electrochemsci.org

Influence of dodecyl sulfate anions doped hydroxide precursor on enhanced electrochemical properties of $LiNi_xCo_yMn_{1-x-y}O_2$ as lithium-ion battery cathodes

Fanghui Tian[1], Xuecheng Fan[1], Qiang Wang[2], Xiao Ouyang[2,], Hao Wei[2], Qiang Shen[1,*]*

[1] Key Laboratory for Colloid and Interface Chemistry of Education Ministry, School of Chemistry and Chemical Engineering, Shandong University, Jinan 250100, China.
[2] Key Laboratory of Superlight Material and Surface Technology of Education Ministry, College of Material Science and Chemical Engineering, Harbin Engineering University, Harbin 150001, China.
[*]E-mail: qshen@sdu.edu.cn oyx1028@hrbeu.edu.cn

Received: 6 June 2020 / *Accepted:* 16 July 2020 / *Published:* 31 August 2020

Lithium-containing nickel-cobalt-manganese ternary transition metal oxides (e.g., $LiNi_xCo_yMn_{1-x-y}O_2$, abbreviated as NCM) may combine the lithium extraction/insertion advantages of $LiCoO_2$, $LiNiO_2$ and $LiMnO_2$ "single-component" cathode materials because of a well-known synergistic effect at the optimal Ni:Co:Mn molar ratio of 1:1:1. This paper deals with optimized preparation and enhanced electrochemical properties of $LiNi_xCo_yMn_{1-x-y}O_2$ cathode material modified by the addition of anionic surfactant (i.e., sodium dodecyl sulfate SDS) into the hydroxide-precursor precipitation system of equimolar-ratio divalent transition metal sulfates. In the absence and presence of additive SDS, the finally resulting products of NCM and SDS-NCM show the leakage of elemental Co in each formula $LiNi_xCo_yMn_{1-x-y}O_2$, and their crystallites possess an average particle size of 450 ± 100 and 250 ± 40 nm, respectively. This modification makes a relatively high SO_4^{2-} content in SDS-NCM with the better electrochemical properties (e.g., capacity ~135.4 mAh g^{-1}, at 20 mA g^{-1}, in the 150th cycle) than those of NCM (capacity ~93.8 mAh g^{-1}, at 20 mA g^{-1}, in the 150th cycle). In a word, both the structure optimization and performance-enhanced mechanism of SDS-NCM are discussed in detail in context.

Keywords: Ternary transition metal hydroxide, anionic surfactant, cathode, lithium-ion batteries.

1. INTRODUCTION

Facile/precise preparation or development of the lithium-ion battery (LIB) cathode materials of nickel, cobalt and/or manganese transition metal oxides in formula $LiMO_2$ (M = Ni, Co, Mn and/or $Ni_xCo_yMn_{1-x-y}$) has been one of hot research topics in recent years, because of the wide application of

$LiCoO_2$ and its performance improvement by the partly replacing elemental Co with elemental Ni and Mn [1,2]. Among the well-recognized Ni-Co-Mn ternary oxides of $LiNi_xCo_yMn_{1-x-y}O_2$ (e.g., x = 0.8, y = 0.1, NCM811; x = 0.4, y = 0.2, NCM424; x = 3/8, y = 2/8, NCM323; x = y = 1/3, NCM111), the equimolar one of NCM111 is one of the best, which has been assigned to an obvious synergistic effect at the optimal Ni:Co:Mn elemental ratio of 1:1:1 [3,4]. That is, changing the values of x and y in formula $LiNi_xCo_yMn_{1-x-y}O_2$ means not only the variation of chemical composition but also the vastly different electrochemical properties for application. Therefore, the precise control of Ni:Co:Mn molar ratio in material preparation is of crucial importance.

In electrochemistry, reversible reactions of Co^{3+}/Co^{4+} and Ni^{2+}/Ni^{4+} cationic redox couples are generally used to explain the high-capacity characteristics of $LiNi_xCo_yMn_{1-x-y}O_2$, while the unchanged Mn^{4+} merely functionalizes to keep its structural stability therein [5]. One of the key drawbacks to limit the large-scale commercial application of these cathode materials is their severe voltage/capacity fade occurring along with the increasing cycle number (or their poor cycling stability) [6]. To solve this problem, several strategies, such as the nanofabrication of NCM series and the surface modification or morphological control of nanocrystallites, have been adopted [7,8]. Taking the morphology/shape controlling nanofabrication of crystalline $LiNi_xCo_yMn_{1-x-y}O_2$ as an example, it can shorten the Li^+ diffusion pathway within bulk cathode, then promote the reversible capacity after a long-term cycling and then alleviate the drawback of voltage/capacity decay to a great extent [9]. If the partial substitution of elemental Co for Mn means the presence of "single-component $LiMnO_2$" in lattice $LiNi_xCo_yMn_{1-x-y}O_2$, cycling-performance improvement of the NCM may be associated with the alleviation of Jahn-Teller effect by prohibiting the Mn^{3+} dissolution in electrolyte solution, and the disproportionation of Mn^{3+} can interpret the emerging of electrochemical 'inert' Mn^{4+} ions.

To prevent the introduction of any heteroatoms, two-step method is generally adopted to synthesize $LiNi_xCo_yMn_{1-x-y}O_2$ in laboratory. Wherein, the first step is a hydroxide co-precipitation reaction of the divalent salts of Ni-, Co- and Mn-based starting materials, and another step deals with an air-atmosphere solid-state reaction between the as-precipitated $M(OH)_2$ (M = $Ni_xCo_yMn_{1-x-y}$) and a similarly pyrolytic lithium salt [10,11]. No matter which kind of water-soluble salts (e.g., acetates, nitrates, chlorides or sulfates) is selected to precipitate the precursor of ternary $M(OH)_2$, the co-precipitation reaction guarantees atomic-scale distribution of each transition metal in the final product. If divalent cations of Ni-, Co- and Mn-based raw materials are completely consumed in $M(OH)_2$ co-preparation, elemental analysis of the final product NCM is unnecessary to assay the Ni:Co:Mn molar ratio in formula $LiNi_xCo_yMn_{1-x-y}O_2$. Perhaps, using water-soluble sulfates for the hydroxide co-precipitation is an exception, and as demonstrated by X. Huang et al, residual sulfate groups at the particles surface of binary hydroxide precursor $Ni_{0.5}Mn_{1.5}(OH)_2$ could be detected, which exerts a great influence on the crystallization habit of corresponding product $LiNi_{0.5}Mn_{1.5}O_4$ [12].

Aside from surface adsorption of the counterions of Ni-, Co- and Mn-based starting materials, experimental parameters, such as precipitant and chelating agent, pH value, time, temperature, stirring and so on, could more or less affect the microstructure, morphology/shape, composition, particle size and its distribution of the ternary hydroxide precursor or corresponding product NCM [13-16]. For example, using $NH_3{\cdot}H_2O$ as chelating agent can induce the formation of $[M(NH_3)_n]^{2+}$ complex ions prior to co-precipitation of the ternary precursor $M(OH)_2$ by sodium hydroxide [17]. According to the room-

temperature solubilities of single-component $Ni(OH)_2$, $Co(OH)_2$ and $Mn(OH)_2$, each kind of cations begins to precipitate from pH 4.0 at 0.1 mol L^{-1} of M^{2+} ions, and during the optimal pH range of 10.5-12.5 for this co-precipitation, solubilities of the three single-component hydroxides are quite different: $Co(OH)_2$ > $Ni(OH)_2$ > $Mn(OH)_2$ [10,18]. Considering the much lower solubility of a divalent metal dodecyl sulfate $M(DS)_2$ than that of $M(OH)_2$ counterpart, anionic surfactant sodium dodecyl sulfate (SDS) can also be used as the co-precipitant of NaOH at an operation temperature lower than its Kraft point of 10°C [19,20]. In view of this, effect of the doping DS^- ions on the structural and electrochemical properties of NCM cathode materials deserves to be conducted.

In this paper, sulfate-based raw materials at the Ni:Co:Mn molar ratio of 1:1:1 are used to precipitate $Ni_{0.33}Co_{0.14}Mn_{0.53}(OH)_2$ and then to produce $LiNi_{0.32}Co_{0.14}Mn_{0.54}O_2$ (NCM) at first, and then anionic surfactant SDS is further added into the co-precipitation system to promote the doping amount of sulfate groups in the modified precursor $Ni_{0.37}Co_{0.15}Mn_{0.48}(OH)_2$ or product $LiNi_{0.36}Co_{0.15}Mn_{0.49}O_2$ (SDS-NCM), aiming to assay the doping of dodecyl sulfate groups into the Ni-Co-Mn ternary hydroxide precursor for the enhanced electrochemical properties of final product $LiNi_xCo_yMn_{1-x-y}O_2$ as LIB cathodes. In context, the possible function of additive SDS, together with the performance-enhanced mechanism of SDS-NCM, are discussed in detail.

2. EXPERIMENTAL

2.1. Nanofabrication of layered $LiNi_xCo_yMn_{1-x-y}O_2$

The above mentioned two-step method is adopted for nanofabrication of the LIB cathode materials of $LiNi_xCo_yMn_{1-x-y}O_2$ [10,11], and the procedure of which is described as below. At first, equimolar Ni-Co-Mn sulfate-based chemicals are dissolved in ultrapure water at 50°C under a vigorous stirring, resulting in a pink solution with a 1.0 mol L^{-1} of all cations. Secondly, the alkaline solution of NaOH (2.0 mol L^{-1}) and NH_4OH (2.0 mol L^{-1}) is dropwise added into this pink solution in half an hour until the final pH 12.0 of supernatant is reached. Thirdly, the co-precipitation reaction system is thermostatically kept under a vigorous stirring at 50°C for 12 h, and then the precipitate is collected by centrifugation, thoroughly rinsed with water and ethanol for 3 times and completely dried at 80°C, resulting in the dark-brown precursor $M(OH)_2$ ($M = Ni_xCo_yMn_{1-x-y}$). Finally, powders of chemical Li_2CO_3 and as-prepared precursor $M(OH)_2$, at the Li:($Ni_xCo_yMn_{1-x-y}$) molar ratio of 1.05:1.00, are thoroughly ball milled and then are subjected to an air-atmosphere solid-state reaction at 500°C for 6 h and then at 900°C for 12 h to obtain NCM nanocrystallites.

For comparison purposes, this procedure is also used to prepare the hydroxide precursor (SDS-precursor) and final product $LiNi_xCo_yMn_{1-x-y}O_2$ (SDS-NCM) in the presence of anionic surfactant SDS. Herein, powdered SDS is added into the pink solution of $NiSO_4$, $CoSO_4$ and $MnSO_4$, at a concentration of 0.05 mol L^{-1}, before the addition of NaOH/NH_4OH alkaline solution, and the processing temperature of co-precipitation reaction is preseted at 50°C because of a no less than 40°C Kraft point of the possibly doped $M(DS)_2$ in the ternary $M(OH)_2$.

2.2. Structural characterization

Scanning electron microscopy (SEM) images are taken using a Gemini 300 instrument with a field emission source at 3 kV, and the attached Bruker Quantax 200 XFlash 6|100 energy dispersive X-ray spectrometry (EDS) is used to estimate the chemical compositions of hydroxide precursors and corresponding products. Powder X-ray diffraction (XRD) data is collected on a PANalytical X'Pert3 powder X-ray diffractometer (Cu-Kα radiation, 40 kV, 40 mA) with the 2θ range of 10-80°. Fourier transform infrared spectroscopy (FT IR) data is conducted on a VERTEX-70 spectrometer (KBr tablet) within the region of 4000-400 cm^{-1} and a resolution of 4 cm^{-1}. Thermogravimetric analysis - differential scanning calorimetry (TGA-DSC) tests are conducted on a thermal analyzer (SDT-Q600) under air atmosphere with a heating step of 10°C min^{-1} from room temperature to 850°C.

2.3. Electrochemical characterization

By casting uniform hydrophilic slurry at the mass ratio of active substance (NCM or SDS-NCM): conductive agent (acetylene black): binder (sodium alginate) of 7:2:1 onto aluminum foil, the aluminum foil is punched into disks (12 mm in diameter) after its complete drying at 80°C, resulting in the working electrodes with an average mass loading of 1.8 ± 0.2 mg cm^{-2}. CR2032-type coin cells are assembled in an argon-filled glove box using lithium foil, nickel foam, Celgard 2300 microporous membrane and commercial LBC 305-01 (1.0 mol L^{-1} $LiPF_6$, ethylene:dimethyl:diethyl carbonates = 1:1:1 in v/v/v) as counter electrode, current collector, separator and electrolyte, respectively.

Galvanostatic charge-discharge tests are conducted on a LAND CT2001A battery system within the electrochemical window of 2.0-4.7 V (vs. Li^+/Li and hereafter) at 30°C. Cyclic voltammetry (CV) measurements are performed on a LK2005A electrochemical workstation at 0.1 mV s^{-1}. Electrochemical impedance spectroscopy (EIS) results are obtained using an EG&G PAR 273A electrochemical workstation with a range of 0.1 MHz - 0.1 Hz and an AC amplitude of 10 mV.

3. RESULTS AND DISCUSSION

3.1. The effect of DS^- doping on the structural properties of precursors and products

According to literature reports [10], herein the co-precipitation formation mechanism of a ternary hydroxide $M(OH)_2$ ($M = Ni_xCo_yMn_{1-x-y}$) can be described by the following equations:

$$M^{2+}(aq.) + nNH_4OH \rightarrow [M(NH_3)_n]^{2+} + nH_2O \quad (1)$$

$$[M(NH_3)_n]^{2+} + 2OH^- + nH_2O \rightarrow M(OH)_2 + nNH_4OH \quad (2)$$

$$[M(NH_3)_n]^{2+} + 2DS^- + nH_2O \rightarrow M(DS)_2 + nNH_4OH \quad (3)$$

Wherein, M^{2+} cations represent all the transition metals ions of divalent nickel, cobalt and manganese sulfates, and equations (1) and (2) reveal the chelation of $NH_3 \cdot H_2O$ and precipitants action of NH_4OH and/or NaOH, respectively. In equation (3), DS^- anions are the head groups of SDS anionic surfactants, which are tentatively used for the doping of DS^- into the precursor $M(OH)_2$.

Because at ~10°C the solubility of single-component $M(DS)_2$ is much lower than that of the hydroxide counterpart, the operation temperature of 50°C is to prevent the possible precipitation of $M(DS)_2$ prior to addition of $NaOH/NH_4OH$ and then to restrain the subsequent transformation of $M(OH)_2$ to $M(DS)_2$ as much as possible [21]. As shown in Scheme 1, prior to the addition of $NaOH/NH_4OH$, the (MSO_4 + SDS) (M = Ni, Co, Mn) solution is visually clear, mainly showing the pink of aqueous Co^{2+} ions in color. As for the precipitation system of the ternary $M(OH)_2$ in the presence of SDS, shortly after the complete addition of $NaOH/NH_4OH$ the resulting suspension mainly displays the color of blue-green, being assigned to the color matching of laurel-green $Ni(OH)_2$, pink $Co(OH)_2$ and white $Mn(OH)_2$ at the equimolar ratio of Ni:Co:Mn. Actually, this phenomenon is similar to that in the absence of SDS, and at the end of the precipitation reaction, the color of elemental Co can also be recognized for the finally instant supernatant at pH ~10.9. Therefore, these confirm the higher solubility of $Co(OH)_2$ than that of $Ni(OH)_2$ or $Mn(OH)_2$, indicating that the Ni:Co:Mn molar ratio of sulfate-based starting materials could hardly be used to that of the ternary $M(OH)_2$.

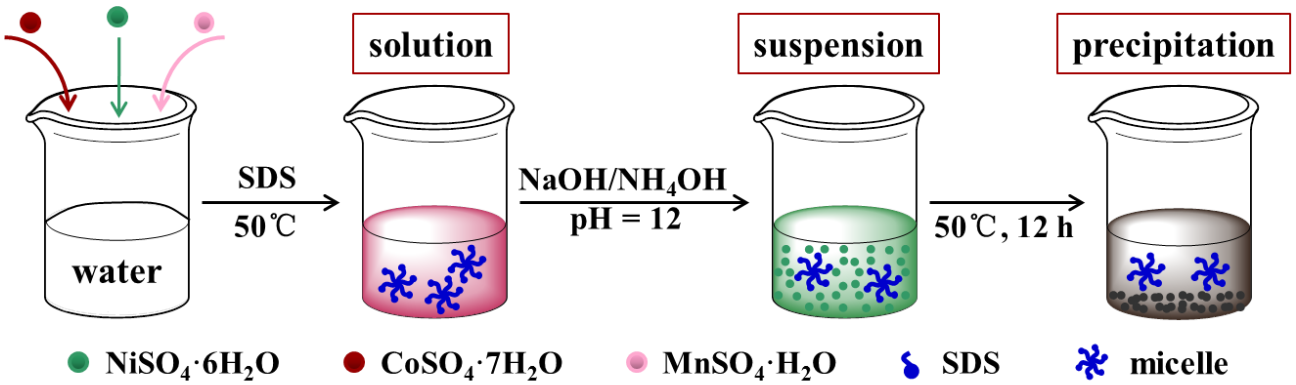

Scheme 1. Schematic diagram for the formation process of SDS-precursor.

In consideration of water-soluble feature of the three sulfates, the adsorption of sulfate groups onto the particles surface of a hydroxide precursor could hardly be neglected because of strong electrostatic interactions. This is reason why, when nitrate-based starting materials are selected for the materials preparation, the Ni:Co:Mn molar ratio of either the ternary $M(OH)_2$ or the final NCM is 1:1:1 (Data omitted). It should be mentioned that critical micellization concentration of the possible formed $M(DS)_2$ is close to that of SDS (i.e., ~9.0×10^{-3} mol L^{-1}), indicating that, in case of the in-situ formation of $M(DS)_2$, it could be solubilized by the surfactant micelles [22]. Even if no DS^- anions are doped into the inner part of $M(OH)_2$ particles, dispersion action of the anionic surfactants can also make hydrocarbon chain-containing head groups (i.e., DS^- ions) being anchored onto the particles surface of $M(OH)_2$.

EDS measurements reveal that both as-obtained $M(OH)_2$ precursors and corresponding $LiNi_xCo_yMn_{1-x-y}O_2$ products contain elemental S. In detail, in the absence and presence of SDS, the estimated S/M elemental ratios of the two ternary $M(OH)_2$ (i.e., precursor and SDS-precursor) are 3.0 and 7.1, whereas those of corresponding products NCM and SDS-NCM are calculated as 1.8 and 3.1, respectively. By comparison, this qualitatively indicates that the presence of anionic surfactant SDS in

the co-precipitation system introduces a relatively more amount of sulfate groups into the resulting SDS-NCM product. Moreover, in the absence of SDS, the estimated Ni:Co:Mn molar ratios of the precursor and corresponding NCM are 0.33:0.14:0.53 and 0.32:0.14:0.54, and in the presence of SDS, those of the SDS-precursor and corresponding SDS-NCM are 0.37:0.15:0.48 and 0.36:0.15:0.49, respectively. By comparing the ternary $M(OH)_2$ precursor with its corresponding NCM product, their slight difference in the S/M elemental ratio or the Ni:Co:Mn molar ratio can be simply attributed to the effect of high-temperature treatment on the decomposition of hydrocarbon chains of these $M(OH)_2$-adsorbed surfactant ions.

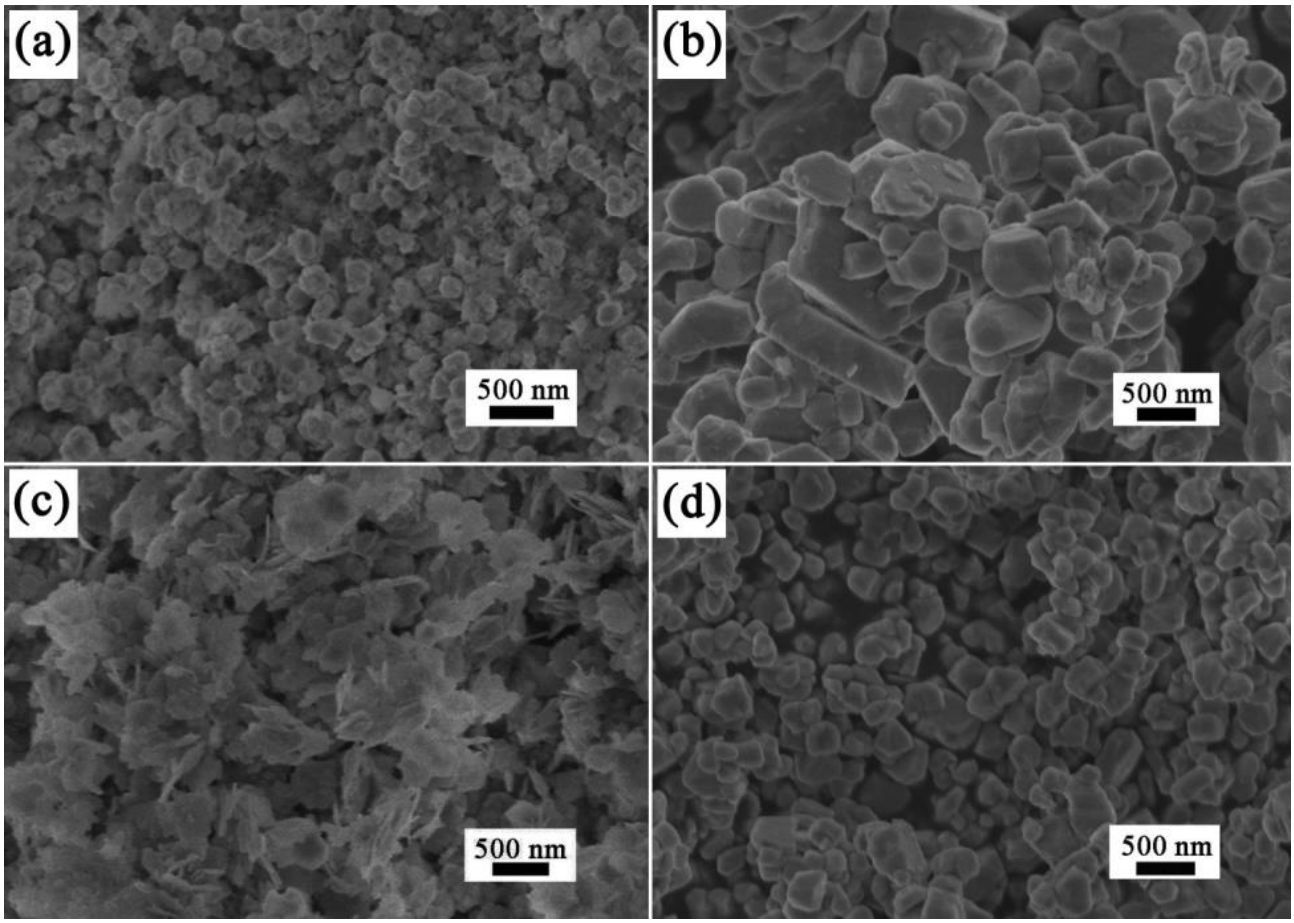

Figure 1. SEM images of (left) ternary $M(OH)_2$ precursors and (right) corresponding products $LiNi_xCo_yMn_{1-x-y}O_2$ obtained in the (a, b) absence and (c, d) presence of SDS, respectively.

In the absence of SDS, as-precipitated particles of the ternary $M(OH)_2$ precursor acquire a relatively uniform dimension at nanoscale (Figure 1a), and crystallites of the corresponding NCM (i.e., $LiNi_{0.32}Co_{0.14}Mn_{0.54}O_2$) are polydisperse in dimension, ranging from dozens of nanometers to several micrometers (Figure 1b). By statistical analysis, particle size of the precursor is about ~175 nm, whereas the average particle size of NCM is estimated at 450 ±100 nm. By comparison, the presence of SDS induces the formation of ultrathin nanosheets of the SDS-precursor with an estimated thickness of ~25 nm, indicating that DS^- anions in the co-precipitation system of hydroxide functionalize as the active sites for the nucleation of ternary $M(OH)_2$ (Figure 1c) [22]. Interestingly, even after the complete

decomposition of the hydrocarbon chains of these $M(OH)_2$-adsorbed surfactant ions under air-atmosphere at 900°C for 12 h, the residual sulfate groups in the solid-state reaction system of SDS-precursor and Li_2CO_3 still play an important role in the nucleation and crystal growth of SDS-NCM (i.e., $LiNi_{0.36}Co_{0.15}Mn_{0.49}O_2$) with an average particle size of 250 ± 40 nm (Figure 1d).

XRD pattern of each ternary $M(OH)_2$ precursor (Figure 2a), obtained in the absence and presence of SDS, mainly shows a sharp diffraction signal at the 2Thelta position of ~19°, and this diffraction peak may be assigned to a (00*l*) crystal plane of the layered transition metal hydroxides [23,24]. The presence of SDS into co-precipitation system does not induce the 2Thelta position shift of (00*l*)-face diffraction, revealing that DS^- anions mainly localize at surface of the ternary $M(OH)_2$ crystallites. XRD patterns of the final products NCM and SDS-NCM (Figure 2b) match well with the standard reflection data of hexagonal $LiNiO_2$ (R-3m space group, JCPDS No. 09-0063; a = b = 2.878 Å, c = 14.190 Å; α = β = 90°, γ = 120°; v = 101.8 $Å^3$) [25].

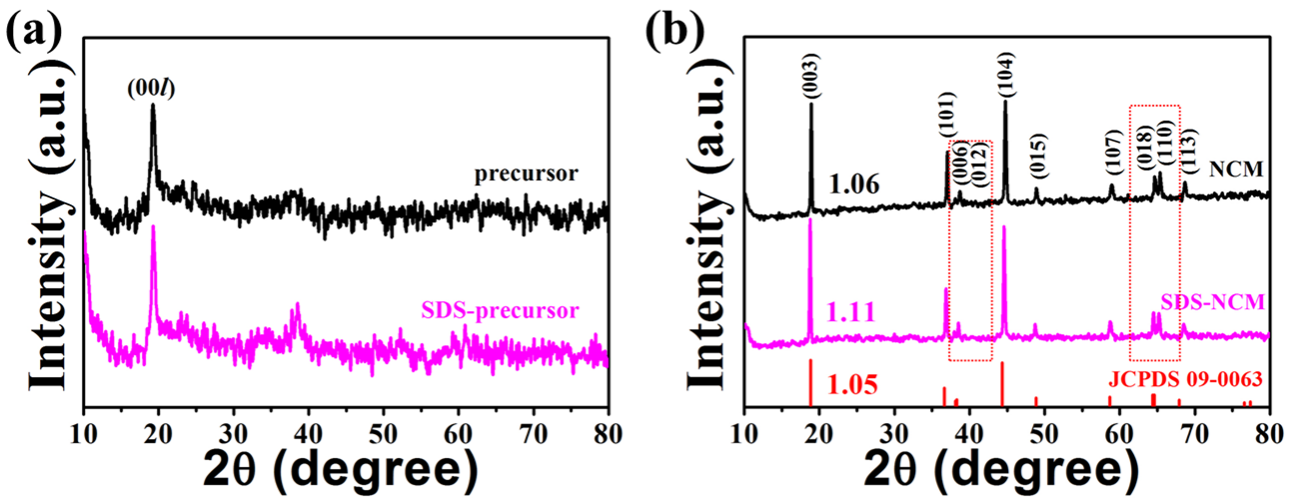

Figure 2. XRD patterns of (a) as-precipitated ternary $M(OH)_2$ precursors and (b) corresponding products $LiNi_xCo_yMn_{1-x-y}O_2$.

In Figure 2b, splitting of the adjacent diffraction peaks of (006)/(012) at ~38° and (018)/(110) at ~65° is indicative of a well-organized layered structure of $LiMO_2$ (M = Ni, Co and/or Mn) [26,27]. The peak intensity ratio between (003) and (104) crystal planes (i.e., $I_{(003)}/I_{(104)}$) could be used to denote both structural ordering and cation mixing, and the higher value of $I_{(003)}/I_{(104)}$ means the better structural ordering and the lower cation mixing [28,29]. As marked in Figure 2b, the $I_{(003)}/I_{(104)}$ ratio of NCM (1.06) is close to that of standard $LiNiO_2$ (1.05) but is obviously lower than that of SDS-NCM (1.11). If the slight $I_{(003)}/I_{(104)}$-ratio difference between $LiNiO_2$ and NCM is associated with a slightly doping of sulfate groups, the higher $I_{(003)}/I_{(104)}$ value of SDS-NCM than that of NCM means the higher content of residual sulfate groups in SDS-NCM. Importantly, these indicate that the doping of DS^- anions into SDS-precursor exert a great influence on the crystallization habit of corresponding product SDS-NCM, coinciding well with the literature results that the residual sulfate groups of precursor $Ni_{0.5}Mn_{1.5}(OH)_2$ could modify the crystallization habit of product $LiNi_{0.5}Mn_{1.5}O_4$ [12].

In the absence of SDS, as-obtained ternary $M(OH)_2$ precursor presents the FT IR characteristics of adsorbed H_2O and functional OH^-, between 3663 and 2610 cm^{-1}, non-removable SO_4^{2-} groups, at 1190, 1107 and 867 cm^{-1}, and M-O framework, within 700-400 cm^{-1} (Figure 3a). Also in Figure 3a, FT IR spectrum of SDS-precursor further shows the typical hydrocarbon chain signals of doped DS^- anions within 3000-2800 cm^{-1}, and by comparison the no less than 40-cm^{-1} red shift of the sulfate groups confirms the doping of DS^- anions with SDS-precursor [12]. TGA-DSC behaviors of the ternary $M(OH)_2$ precursor obtained in the absence of SDS mainly display an initial weight loss of ~3.3 wt% before 100°C and the subsequent weight loss of ~18.4 wt% within 100-500°C (Figure 2b). Wherein, the first weight loss can be assigned to the evaporation of adsorbed H_2O, and another one may relate to the transformation of $M(OH)_2$ to MO with a theoretical value of ~19.7 wt%. Also in Figure 2b, the SDS-precursor's TGA-DSC behavior comparatively gives the stronger endothermic peak around 246.0°C and the bigger weight loss of 24.7 wt% within 100-500°C, and these can be attributed to the presence of DS^- anions with a doping amount of ~7.7 wt%.

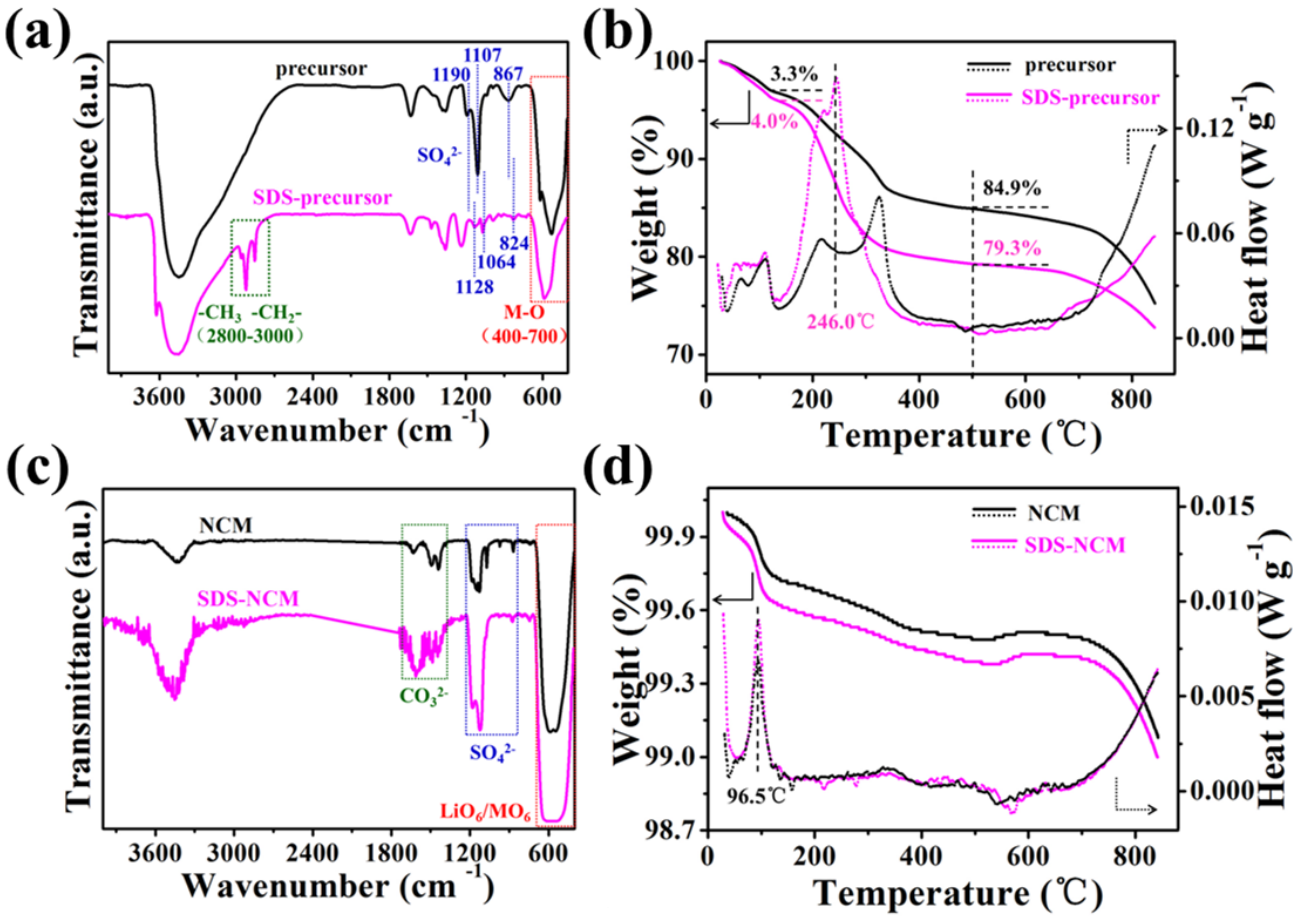

Figure 3. (left) FT IR spectra and (right) TGA-DSC profiles of (a, b) ternary $M(OH)_2$ precursors and (c, d) corresponding products $LiNi_xCo_yMn_{1-x-y}O_2$, respectively.

As for the two final products of NCM and SDS-NCM, each of them exhibits the FT IR characteristics of adsorbed H_2O around ~3420 cm^{-1}, CO_3^{2-} functional group within 1700-1320 cm^{-1},

SO_4^{2-} functional group within 1210-850 cm^{-1} and LiO_6/MO_6 framework between 700 and 400 cm^{-1} (Figure 3c) [30]. As demonstrated in literature [31], the emerging of the adsorption bands of adsorbed H_2O and functional group CO_3^{2-} is common for lithium-containing transition metal oxides, which originates from the room-temperature reaction of Li_2O with moisture and CO_2 under the air atmosphere. TGA-DSC measurements of NCM and SDS-NCM only reveal the evaporation of adsorbed moisture around 96.5°C, which indicates the complete decomposition of alkyl chains of doped DS^- anions during the formation process of $LiNi_xCo_yMn_{1-x-y}O_2$ cathode materials (Figure 3d).

3.2 The enhanced electrochemical properties of SDS-NCM

When NCM or SDS-NCM is applied as an active substance of LIB cathode, its initial 5 CV curves, recorded at 0.01 mV s^{-1} within 2.0-4.7 V, are presented in Figure 4a or b, showing that, except for the 1st-cycle profile, the other 4-cycle CV curves overlap with each other. Discrepancy of the 1st-cycle CV curve can be surely assigned to the irreversible formation of solid/electrolyte interphase (SEI) films [32,33], whereas shape consistence of the other 4-cycle curves suggests the good electrochemical reversibility for the lithium extraction-insertion of each product [33,34].

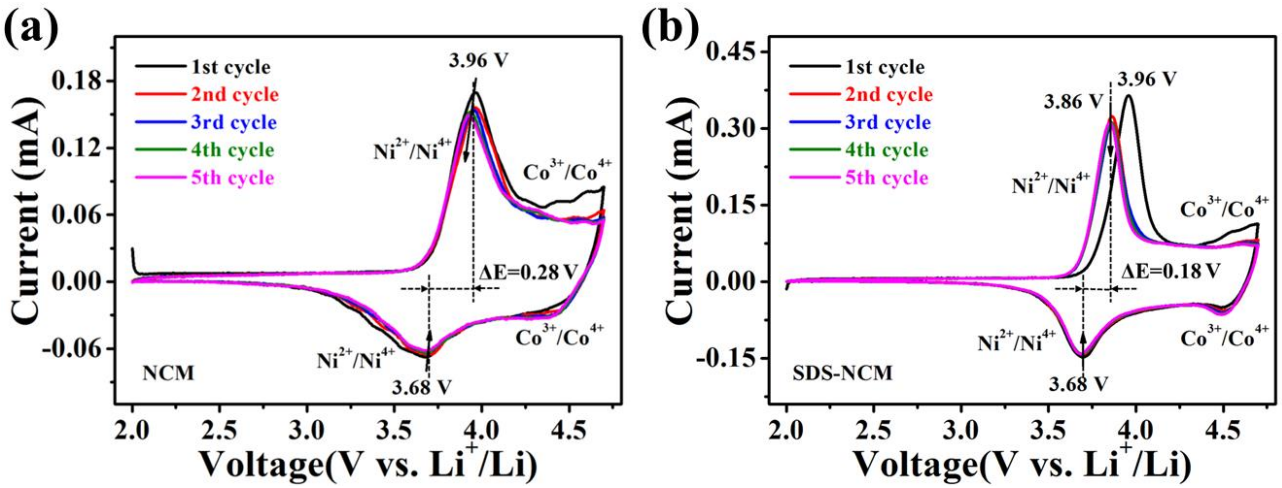

Figure 4. CV curves of (a) NCM and (b) SDS-NCM electrodes obtained at 0.01 mV s^{-1}.

As well demonstrated in literatures [35], in Figure 4a or b the 2nd-cycle CV anodic/cathodic peaks at 3.96/3.68 V (or 3.86/3.68 V) correspond to the Ni^{2+}/Ni^{4+} redox process of NCM or SDS-NCM, while the absence of redox peaks around 3 V and the weak redox peaks around 4.5 V prove the absence of Mn^{3+}/Mn^{4+} redox signals and the relatively low electrochemical activity of Co^{3+}/Co^{4+} redox reactions, respectively. Also, the Ni^{2+}/Ni^{4+} anodic peak area of SDS-NCM (i.e., 0.079 mA·V) in the 3rd-cycle CV curve is almost as twice as that of NCM (i.e., 0.042 mA·V), meaning the higher electrochemical activation of SDS-NCM by comparison.

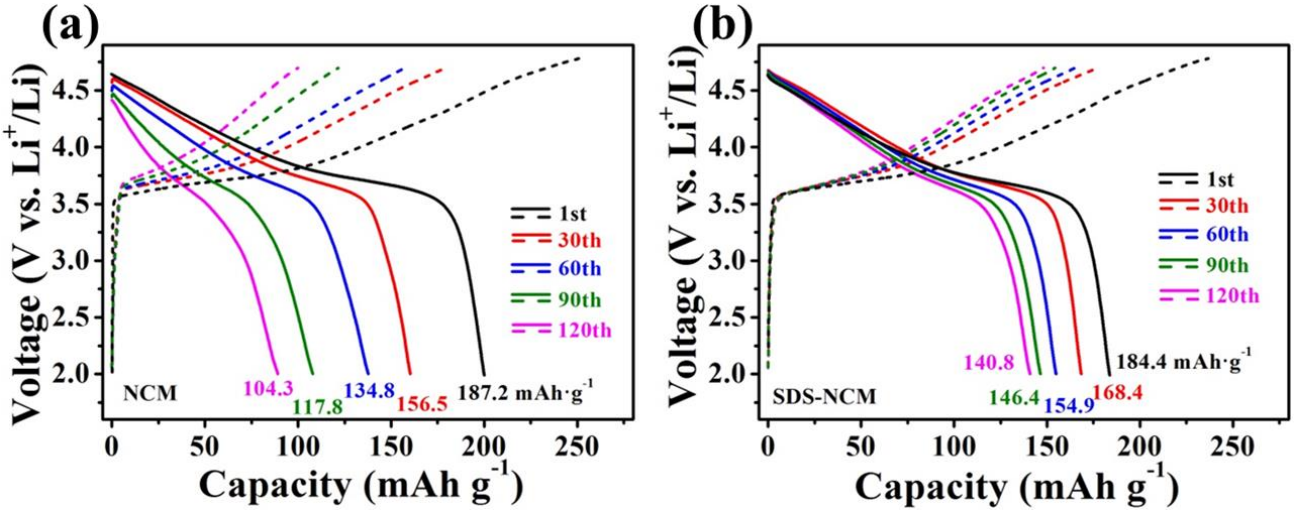

Figure 5. Charge-discharge profiles of (a) NCM and (b) SDS-NCM electrodes obtained at the current density of 20 mA g^{-1}, respectively.

If the peak potential (or peak position in voltage) difference of ΔE between the anodic and cathodic peaks of Ni^{2+}/Ni^{4+} redox couple is indicative of the electrode polarization degree of a cathode herein, as labeled in Figure 4 the ΔE value of NCM electrode (i.e., 0.28 V) higher than that of SDS-NCM cathode (i.e., 0.18 V) means the higher electrode polarization of NCM [32-34]. Therefore, the more amounts of residual SO_4^{2-} groups in product $LiNi_xCo_yMn_{1-x-y}O_2$ is benefit not only to improve its electrochemical activation but also to cut down its electrode polarization.

Within 2.0-4.7 V at 20 mA g^{-1}, the 1st, 30th, 60th, 90th and 120th galvanostatic charge-discharge (GCD) curves of NCM and SDS-NCM are shown in Figure 5a and b, respectively. There are no significant differences for both the initial discharge capacity and the initial Coulombic efficiency between NCM (187.2 mAh g^{-1}, 78.2%) and SDS-NCM (184.4 mAh g^{-1}, 77.9%) (Figure 5a, b). Generally, a low initial Coulombic efficiency of working electrode is due to the formation of SEI films in the 1st GCD cycle [36,37], and along with the increase of cycle number, thereafter the irreversible capacity loss in each cycle has been recognized as an "inherent" feature of $LiNi_xCo_yMn_{1-x-y}O_2$ based cathode materials. As marked in Figure 5a and b, in the 30th, 60th, 90th and 120th cycles the reversible specific capacities of NCM are 156.5, 134.8, 117.8 and 104.3mAh g^{-1}, while those of SDS-NCM are 168.4, 154.9, 146.4 and 140.8 mAh g^{-1}, respectively.

Comparing Fig. 5a with b visually exhibits a "capacity-conflicting" phenomenon that, in the 1st cycle the discharge capacity of SDS-NCM is slight lower than that of NCM, but in the 30th, 60th, 90th or 120th cycle, the specific value of SDS-NCM is obviously higher than that of NCM. In fact, this conflict can be reasonably explained by the capacity decay per cycle or by the change of midpoint discharge potential therein. From the 30th to 120th cycle, the capacity decay rates of NCM and SDS-NCM are calculated as 0.58 and 0.30 mAh g^{-1} per cycle, and midpoint discharge potentials of the two cathodes change from 3.87 to 3.73 V and from 3.87 to 3.84 V, respectively. Importantly, these are in agreement with the CV results shown in Figure 4 that residual SO_4^{2-} in a $LiNi_xCo_yMn_{1-x-y}O_2$ product may be useful to slow down its capacity fade upon the continuous cycling.

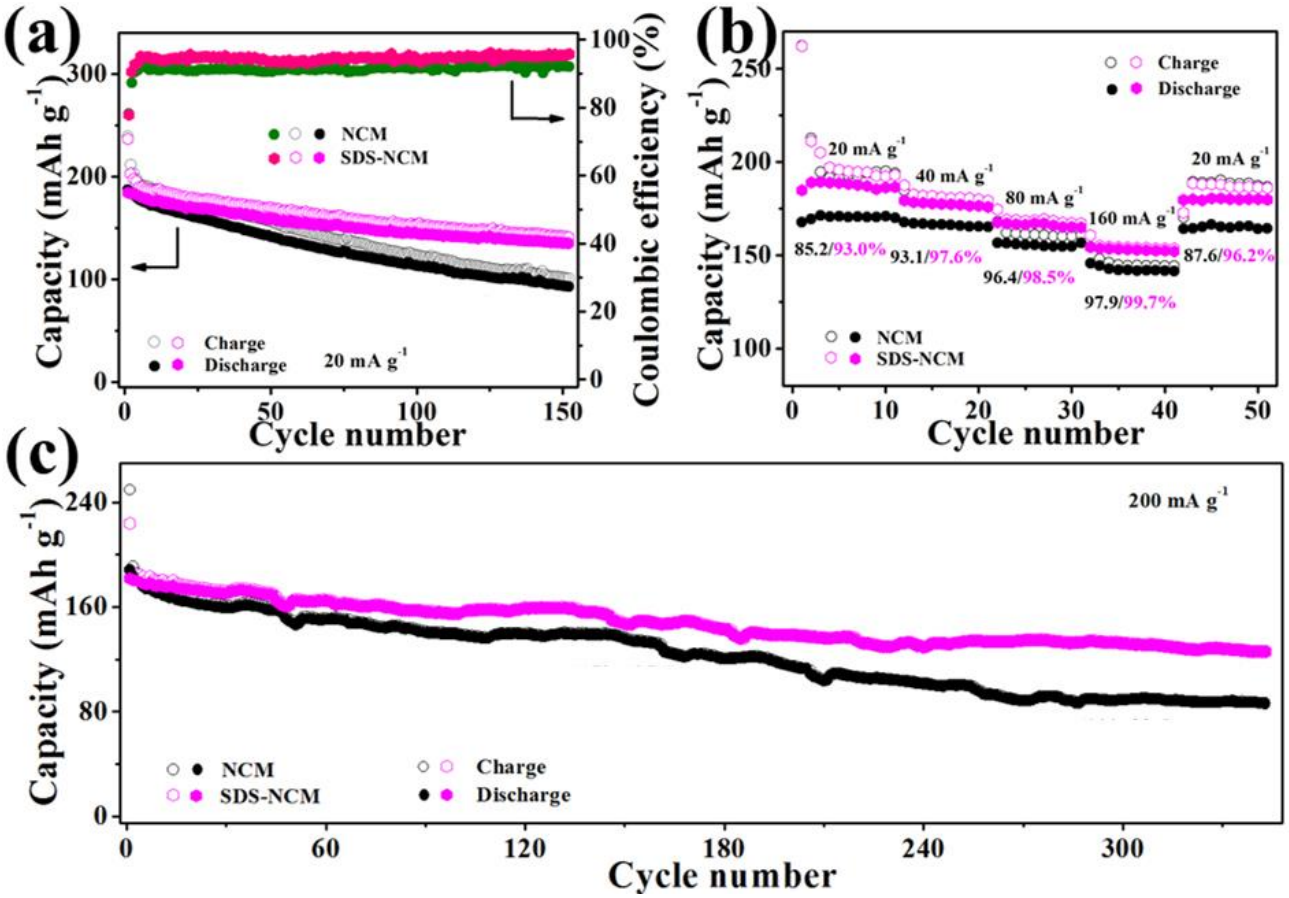

Figure 6. (a) Cycling stabilities, (b) rate capabilities and (c) long-term cycling performances of NCM and SDS-NCM cathodes. In panel (b), the Coulombic efficiency of each cathode at a current density is also marked therein.

Within the electrochemical window of 2.0-4.7 V at 20 mA g^{-1}, cycling and rate performances of NCM and SDS-NCM are comparatively presented in Figure 6a and b, respectively. As for the Coulombic efficiency of NCM or SDS-NCM in each cycle (Figure 6a), it gradually increases from 78.2% or 77.9% in the 1st cycle to 91.0% or 93.2% in the 4th cycle and then to a stable value of 91.5% or 94.6% in the 5th cycle and thereafter. Also, the discharge capacities of NCM (i.e., 187.2, 185.0 and 183.8 mAh g^{-1}) in the initial three cycles are always bigger than those of SDS-NCM (i.e., 184.4, 183.7 and 183.5 mAh g^{-1}) correspondingly. In the 4th cycle and thereafter, the comparisons are reverse: the reversible capacity of NCM or SDS-NCM gradually decreases from 179.8 or 182.4 mAh g^{-1} in the 4th cycle to a value of 93.8 or 135.4 mAh g^{-1} in the 150the cycle (Figure 6a). According to the discharge capacity in the 2nd cycle, in the 150th cycle the capacity retention rate of NCM is as low as 50.7%, while the capacity retention rate of SDS-NCM is calculated as 73.7%. Therefore, from the view point of Coulombic efficiency or capacity retention rate, the cycling performance of SDS-NCM is better than that of NCM.

When the applied current rate (C-rate) of a $LiNi_xCo_yMn_{1-x-y}O_2$ cathode gradually increases from 20 to 160 mA g^{-1}, discharge capacity of the electrode decreases correspondingly. Subsequently, when C-rate returns back from 160 to 20 mA g^{-1} again, the discharge capacity of each electrode almost recovers to the same value as before (Figure 6b). These are indicative of a good rate capability of NCM or SDS-

NCM. Visually, the discharge capacity of SDS-NCM in each cycle is always bigger than that of NCM at each operating C-rate, and as marked in Figure 6b, the calculated Coulombic efficiency of SDS-NCM is also bigger than that of NCM at each operating C-rate. This means the more outstanding rate performance of SDS-NCM than that of NCM, being assigned to the better Li^+-ion diffusion kinetics of lattice SDS-NCM with the more amounts of residual SO_4^{2-} therein.

To assay the practical applicability of SDS-NCM, the long-term cycling performances of NCM and SDS-NCM, operated at a high C-rate of 200 mA g^{-1}, are comparatively shown in Figure 6c. From Figure 6c, it is similar to find that: (i) in the 1st and 2nd cycles the discharge capacities (188.3 and 183.5 mAh g^{-1}) of NCM are higher than those (181.9 and 180.6 mAh g^{-1}) of SDS-NCM, and in each of the subsequent cycles the reversible capacity of NCM is always smaller than that of SDS-NCM; (ii) in the 300th cycle, both the residual specific capacity (131.9 mAh g^{-1}) of SDS-NCM and the capacity retention rate (73.0%) calculated according to the discharge capacity in the 2nd cycle are much bigger than those (88.6 mAh g^{-1} and 48.3%) of NCM, respectively.

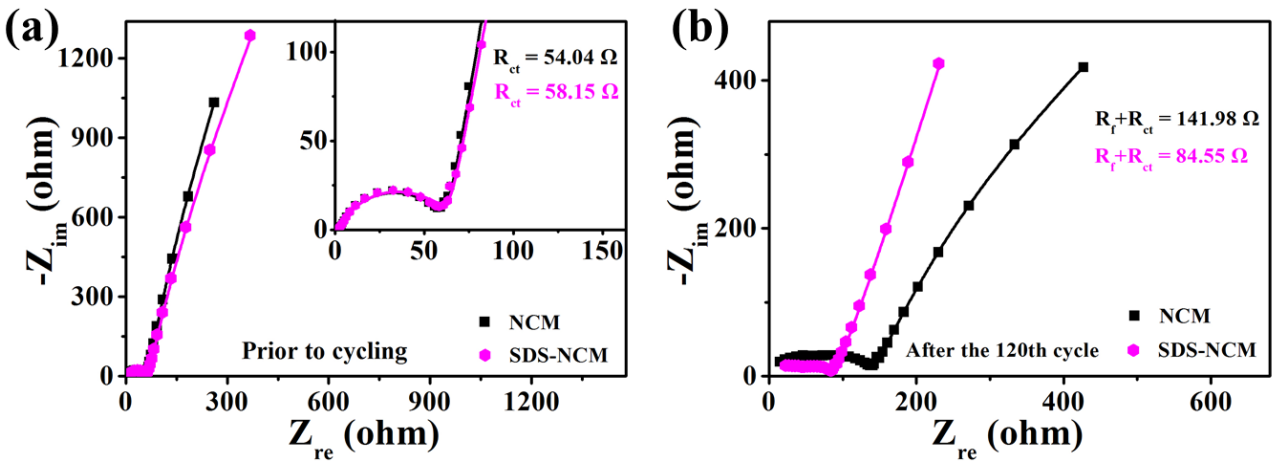

Figure 7. Nyquist plots of NCM and SDS-NCM electrodes obtained under different electrochemical states: (a), at open-circuit voltage; (b), after the continuous 120 cycles at 20 mA g^{-1}.

Aside from the different chemical compositions (i.e., the different Ni:Co:Mn molar ratio), the electrochemical properties (e.g., cycling performance and rate capability) of SDS-NCM better than those of NCM could be simply associated with the smaller average particle size of SDS-NCM induced by the artificially increasing content of doped SO_4^{2-} in lattice structure. That is, neither the literature-demonstrated comprehensive effect of doped SO_4^{2-} on crystallization habit of $LiNi_xCo_yMn_{1-x-y}O_2$ nor the presently unknown positive effect of doped SO_4^{2-} on the high-performance mechanism of SDS-NCM (i.e., $LiNi_{0.36}Co_{0.15}Mn_{0.49}O_2$) could be neglected. Also, to explain the comparatively "capacity-conflicting" phenomenon that the discharge capacity of NCM is bigger than that of SDS-NCM in the initial several cycles and in each of the subsequent cycle this comparison is reverse (Figure 5, 6a or 6c), EIS tests of the two cathodes are performed under different electrochemical states (Figure 7).

Table 1. The comparative electrochemical performances of $LiNi_xCo_yMn_{1-x-y}O_2$ cathode materials in literature reports.

Additive	Chemical composition	Electrochemical performance		Ref.
		Current density ($mA\ g^{-1}$)	Reversible capacity ($mAh\ g^{-1}$)	
H_3BO_3	$LiNi_{0.8}Co_{0.15}Al_{0.05}O_2$	360	200th cycle, 155.1	1
/	$LiNi_{0.6}Co_{0.2}Mn_{0.2}O_2$	40	100th cycle, ~130	3
$C_6H_8O_7 \cdot H_2O$	$LiNi_{0.5}Co_{0.3}Mn_{0.2}O_2$	36	40th cycle, 179.0	10
/	$LiNi_{1/3}Co_{1/3}Mn_{1/3}O_2$	80	160th cycle, 136.2	11
/	$LiNi_{0.85}Co_{0.05}Mn_{0.1}O_2$	36	100th cycle, 165.4	13
/	$LiNi_{1/3}Co_{1/3}Mn_{1/3}O_2$	40	100th cycle, 148.8	14
/	$LiNi_{1/3}Co_{1/3}Mn_{1/3}O_2$	28	73th cycle, 104.9	15
/	$LiNi_{1/3}Co_{1/3}Mn_{1/3}O_2$	180	50th cycle, 155.0	24
PPy[1]	$LiNi_{1/3}Co_{1/3}Mn_{1/3}O_2$	40	300th cycle, 121.3	25
/	$LiNi_{0.8}Co_{0.1}Mn_{0.1}O_2$	360	100th cycle, 155.0	26
TEA[2]	$LiNi_{1/3}Co_{1/3}Mn_{1/3}O_2$	36	100th cycle, 136.2	27
V_2O_5-SDBS[3]	$LiNi_{1/3}Co_{1/3}Mn_{1/3}O_2$	100	100th cycle, 192.9	28
/	$LiNi_{1/3}Co_{1/3}Mn_{1/3}O_2$	20	50th cycle, 153.0	30
$LiAlO_2$	$LiNi_{0.8}Co_{0.1}Mn_{0.1}O_2$	100	100th cycle, 158.8	33
$NH_4H_2PO_4$	$LiNi_{0.6}Co_{0.2}Mn_{0.2}O_2$	90	100th cycle, 158.8	34
KH550[4]	$LiNi_{0.6}Co_{0.2}Mn_{0.2}O_2$	180	50th cycle, 182.0	38
SDS	$LiNi_{0.32}Co_{0.14}Mn_{0.54}O_2$	200	50th cycle, 164.6 100th cycle, 154.7 300th cycle, 131.9	This work

Note: [1] PPy - polypyrrole; [2] TEA - triethanolamine; [3] SDBS - dodecyl benzene sulfonate; [4] KH550 – silane coupling agents

From the comparative Nyquist plots of the two cathodes at open-circuit voltage, the estimated values of charge-transfer resistance (R_{ct}) are 54.0 and 58.2 Ω for NCM and SDS-NCM, respectively (Figure 7a). Shortly after the 120th cycles at 20 mA g^{-1}, the sum values of surface-film resistance (R_f) and charge-transfer resistance R_{ct} (i.e., $R_f + R_{ct}$) of NCM and SDS-NCM are 141.98 and 84.55 Ω in sequence (Figure 7b). Generally, the higher value of R_{ct} or ($R_f + R_{ct}$), the lower degree of electrode polarization and the higher electrochemical performance of working electrode [38,39]. Moreover, both the electrochemical inert feature of residual SO_4^{2-} and its possibly strong electrostatic interactions with transition metal ions should be considered to relate with the structural stability of SO_4^{2-}-doped $LiNi_xCo_yMn_{1-x-y}O_2$ upon the continuous cycling. In brief, these may cooperatively explain the capacity-conflicting phenomena between NCM and SDS-NCM, and especially the long-term high-performance behavior of SDS-NCM suggest its potential application in future.

According to the chemical compositions and electrochemical properties of $LiNi_xCo_yMn_{1-x-y}O_2$ cathode materials summarized in Table 1, by comparison both the long-term cycling stability and high-

rate capability of SDS-NCM electrode are not bad. As for the comparative results shown in Table 1, another three aspects should be emphasized: (i) the dopant of sulfate group is electrochemical inert by comparison with the electrochemical activity of a polyanionic group of BO_3^{3-}, VO_4^{3-}, PO_4^{3-} or SiO_3^{2-} [1,28,34,38]; (ii) the addition of an organic or conductive additive could more or less modify the reversible lithium extraction-insertion kinetics of $LiNi_xCo_yMn_{1-x-y}O_2$ cathode [10,25,27]; (iii) herein the doping of DS^- is subjectively used to highlight the incomplete removal of sulfate groups from the precipitate of ternary precursor $Ni_xCo_yMn_{1-x-y}(OH)_2$, and the higher electrochemical properties of SDS-NCM than those of NCM indicate a positive effect of residual SO_4^{2-} groups therein.

4. CONCLUSIONS

In summary, in the presence of anionic surfactant SDS, the precipitation reaction between the divalent Ni-Co-Mn sulfates and ammonia-containing sodium hydroxide is used to highlight the incompletely removal of SO_4^{2-} from the ternary hydroxide precursor $M(OH)_2$ ($M = Ni_xCo_yMn_{1-x-y}$) obtained in the absence of SDS, and the subsequent air-atmosphere solid-state reaction of the ternary $M(OH)_2$ and Li_2CO_3 unexpectedly results in the different chemical compositions of $LiNi_xCo_yMn_{1-x-y}O_2$ (i.e., NCM, $LiNi_{0.32}Co_{0.14}Mn_{0.54}O_2$; SDS-NCM, $LiNi_{0.36}Co_{0.15}Mn_{0.49}O_2$) for LIB cathodes. Despite of the uncertain effect of residual SO_4^{2-} on the thermal crystallization habit of $LiNi_xCo_yMn_{1-x-y}O_2$, the doping of DS^- anions with the ternary $M(OH)_2$ (i.e., SDS-precursor) obviously cuts down the average particle size of corresponding product (NCM, 450 $\pm$ 100 nm; SDS-NCM, 250 $\pm$ 40 nm). When comparatively serving as LIB cathode active substances, the modified product of SDS-NCM presents the higher electrochemical properties (e.g., cycling stability, rate capability and long-term duriability) than NCM. Moreover, it is interesting to observe the reproducible capacity-conflicting phenomenon between NCM and SDS-NCM, and this could be assigned to the relatively high R_{ct} of SDS-NCM at open-circuit voltage and to the relatively high electrode polarization of NCM upon cycling.

ACKNOWLEDGEMENTS
Authors in Shandong University thank the financial support from the National Natural Science Foundation of China (21673131).

References

1. T. Chen, X. Li, H. Wang, X. Yan, L. Wang, B. Deng, W. Ge, M. Qu, *J. Power Sources*, 374 (2018) 1-11.
2. S. Jurng, S.K. Heiskanen, K.W.D.K. Chandrasiri, M.Y. Abeywardana, B.L. Lucht, *J. Electrochem. Soc.*, 166 (2019) A2721-A2726.
3. T.R. Penki, P.K. Nayak, E. Levi, J. Grinblat, Y. Elias, S. Luski, B. Markovsky, D. Aurbach, *ChemElectroChem*, 5 (2018) 1137-1146.

4. C. Liang, F. Kong, R.C. Longo, S. Kc, J.-S. Kim, S. Jeon, S. Choi, K. Cho, *J. Phys. Chem. C*, 120 (2016) 6383-6393.
5. J. Baboo, H. Park, J. Song, S. Kin, J.Jo, D. Pham, V. Mathew, Z. Xiu, J. Kim, *Electrochim. Acta*, 224 (2017) 243-250.
6. J. Kasnatscheew, M. Evertz, B. Streipert, R. Wagner, S. Nowak, I. Laskovic, M. Winter, *J. Phys. Chem. C*, 121 (2017) 1521-1529.
7. S. Guo, B. Yuan, H. Zhao, Y. Shen, C. Sun, T. Chen, W. Sun, J. Wu, B. Zheng, W. Zhang, S. Li, F. Huo, *Nano Energy*, 58 (2019) 673-679.
8. W. Li, B. Song, A. Manthiram, *Chem. Soc. Rev.*, 46 (2017) 3006-3059.
9. T.-F. Yi, J. Mei, Y.-R. Zhu, *J. Power Sources*, 316 (2016) 85-105.
10. K.-Mo. Nam, H.-J. Kim, D.-H. Kang, Y.-S. Kim and S.-W. Song, *Green Chem.*, 00 (2013) 1-3.
11. Z. Yang, J. Lu, D. Bian, W. Zhang, X. Yang, J. Xia, G. Chen, H. Gu, G. Ma, *J. Power Sources*, 272 (2014) 144-151.
12. B. Chen, L. Ben, Y. Chen, H. Yu, H. Zhang, W. Zhao, X. Huang, *Chem. Mater.*, 30 (2018) 2174-2182.
13. Y. Liu, W.-L. Yao, C. Lei, Q. Zhang, S.-W. Zhong, Z.-Q. Yan, *J. Electrochem. Soc.*, 166 (2019) A1300-A1309.
14. H. Wang, Y. Wei, J. Wang, D. Long, *Electrochim. Acta*, 269 (2018) 724-732.
15. W.-B. Hua, B. Schwarz, M. Knapp, A. Senyshyn, A. Missiul, X. Mu, S. Wang, C. Kübel, J. R. Binder, S. Indris, H. Ehrenberg, *J. Electrochem. Soc.*, 166 (2019) A5025-A5032.
16. Y. Yang, S. Xu, M. Xie, Y. He, G. Huang, Y. Yang, *J. Alloy Compd.*, 619 (2015) 846-853.
17. D. Wang, I. Belharouak, L.H. Ortega, X. Zhang, R. Xu, D. Zhou, G. Zhou, K. Amine, *J. Power Sources*, 274 (2015) 451-457.
18. D. R. Turner, M. Whitfield and A. G. Dickson, *Geochinnuca Cosmochinuca*, 45 (1981) 855-881.
19. S. Miyamoto, *B. Chem. Soc. Jpn*, 33 (1960) 375-379.
20. H. Wang, Q. Shen, X. Li, F. Liu, *Langmiur*, 25 (2009) 3152-3158.
21. Q. Shen, L. Wang, Y. Huang, J. Sun, H. Wang, Y. Zhou, Z. Zhang, D. Wang, *J. Phys. Chem. B*, 110 (2006) 23148-23153.
22. Q. Shen, H. Wei, L. Wang, Y. Zhou, Y. Zhou, Z. Zhang, D. Wang, G. Xu, D. Xu, *J. Phys. Chem. B*, 109 (2005) 18342-18347.
23. X.-Z. Fu, X. Wang, H.-F. Peng, F.-S. Ke, J.-H. Lei, L. Huang, J.-D. Lin, D.-W. Liao, *J. Solid State Electrochem.*, 14 (2009) 1117-1124.
24. W.-B. Hua, X.-D. Guo, Z. Zheng, Y.-J. Wang, B.-H. Zhong, B. Fang, J.-Z. Wang, S.-L. Chou, H. Liu, *J. Power Sources*, 275 (2015) 200-206.
25. L. Zhu, L. Xie, C. Bao, X. Yan, X. Cao, *Int. J. Energy Res.*, (2019) 1-11.
26. X. Lu, X. Li, Z. Wang, H. Guo, G. Yan, X. Yin, *Appl. Surf. Sci.*, 297 (2014) 182-187.
27. J. Zeng, C. Hai, X. Ren, X. Li, Y. Shen, O. Dong, L. Zhang, Y. Sun, L. Ma, X. Zhang, S.Dong, Y. Zhou, *J. Alloy Compd.*, 735 (2018) 1977-1985.
28. M. Yuan, Y. Li, Q. Chen, C. Chen, X. Liu, W. Zeng, R. Wang, S. Xiao, *Electrochim. Acta*, 323 (2019) 134822.
29. Y. Kim, *ACS Appl. Mater. Interfaces*, 4 (2012) 2329-2333.
30. P. Manikandan, P. Periasamy, R. Jagannathan, *J. Power Sources*, 245 (2014) 501-509.
31. Q. Zhang, T. Peng, D. Zhan, X. Hu, *J. Power Sources*, 250 (2014) 40-49.
32. H. Liu, J. Wang, X. Zhang, D. Zhou, X. Qi, B. Qiu, J. Fang, R. Kloepsch, G. Schumacher, Z. Liu, J. Li, *ACS Appl. Mater. Interfaces*, 8 (2016) 4661-4675.
33. W. Tang, Z. Chen, F. Xiong, F. Chen, C. Huang, Q. Gao, T. Wang, Z. Yang, W. Zhang, *J. Power Sources*, 412 (2019) 246-254.
34. Q. Ran, H. Zhao, Q. Wang, X. Shu, Y. Hu, S. Hao, M. Wang, J. Liu, M. Zhang, H. Li, N. Liu, X. Liu, *Electrochim. Acta*, 299 (2019) 971-978.
35. S.-T. Myung, K. Amine, Y.-K. Sun, *J. Power Sources*, 283 (2015) 219-236.

36. R.A. House, U. Maitra, M.A. Perez-Osorio, J.G. Lozano, L. Jin, J.W. Somerville, L.C. Duda, A. Nag, A. Walters, K.J. Zhou, M.R. Roberts, P.G. Bruce, *Nature*, 577 (2020) 502-508.
37. M. Nie, Y.-F. Xia, Z.-B. Wang, F.-D. Yu, Y. Zhang, J. Wu, B. Wu, *Ceram. Int*., 141 (2015) 15185-15192.
38. Y. Chen, S. Tang, S. Deng, T. Lei, Y. Li, W. Li, G. Cao, J. Zhu, J. Zhang, *J. Power Sources*, 431 (2019) 8-16.
39. F. Feng, W.-P. Kang, F.-Q. Yu, H. Zhang, Q. Shen, *J. Power Sources*, 285 (2015) 109-117.